nature

SUPPLEMENTARY INFORMATION

https://doi.org/10.1038/s41586-019-1148-9

In the format provided by the authors and unedited.

Topological superconductivity in a phase-controlled Josephson junction

Hechen Ren[1,2], Falko Pientka[1,3], Sean Hart[1,4], Andrew T. Pierce[1], Michael Kosowsky[1], Lukas Lunczer[5], Raimund Schlereth[5], Benedikt Scharf[6], Ewelina M. Hankiewicz[6], Laurens W. Molenkamp[5], Bertrand I. Halperin[1] & Amir Yacoby[1]*

[1]Department of Physics, Harvard University, Cambridge, MA, USA. [2]Institute for Quantum Information and Matter, California Institute of Technology, Pasadena, CA, USA. [3]Max-Planck-Institut für Physik komplexer Systeme, Dresden, Germany. [4]IBM T. J. Watson Research Center, Yorktown Heights, NY, USA. [5]Physikalisches Institut (EP3) and Institute for Topological Insulators, Universität Würzburg, Würzburg, Germany. [6]Institut für Theoretische Physik und Astrophysik and Würzburg-Dresden Cluster of Excellence ct.qmat, Universität Würzburg, Würzburg, Germany.
*e-mail: yacoby@g.harvard.edu

Supplementary Information for Topological Superconductivity in a Phase-Controlled Josephson Junction

Hechen Ren[1,2], Falko Pientka[1,3], Sean Hart[1,4], Andrew T. Pierce[1], Michael Kosowsky[1], Lukas Lunczer[5], Raimund Schlereth[5], Benedikt Scharf[6], Ewelina M. Hankiewicz[6], Laurens W. Molenkamp[5], Bertrand I. Halperin[1], & Amir Yacoby[1*]

[1]*Department of Physics, Harvard University, Cambridge, MA, USA*

[2]*Institute for Quantum Information and Matter, California Institute of Technology, Pasadena, CA, USA*

[3]*Max-Planck-Institut für Physik komplexer Systeme, Dresden, Germany*

[4]*IBM T. J. Watson Research Center, Yorktown Heights, NY, USA*

[5]*Physikalisches Institut (EP3) and Institute for Topological Insulators, Universität Würzburg, Würzburg, Germany*

[6]*Institut für Theoretische Physik und Astrophysik and Würzburg-Dresden Cluster of Excellence ct.qmat, Universität Würzburg, Würzburg, Germany*

[*]e-mail: yacoby@g.harvard.edu

Contents

List of Figures

1 Device Characterization and Measurement

To characterize our two-dimensional electron gas (2DEG), we fabricate and measure a van der Pauw device on the same HgTe wafer QC0261, using the same metal deposition method described in the main text except replacing the aluminum contacts with gold. By measuring the longitudinal and Hall resistances, we obtain a 2DEG mobility of around 400,000 cm^2/Vs at a density of 1.0×10^{11} cm^{-2}. The longitudinal and Hall resistances are shown respectively in Figure S1a and b.

We fabricate high-quality aluminum/HgTe interface using in-situ ion milling procedure described in our previous works[1,2]. Here we provide a back-of-envelope estimate for the transparency of our Josephson junctions using transport data. For an 800 nm-wide, 4 micron-long junction we made using the same fabrication procedure and with the same thickness of aluminum and sticking layer, the normal resistance $R_N = 200\Omega$. Using a formula for a Josephson junction with two equal interfaces, the resistance is given by $R = \frac{1}{M}\frac{h}{e^2}\left(1 + 2\frac{|r|^2}{|t|^2}\right)$, where M is the number of modes, and t and r are the complex transmission and reflection amplitudes. At an estimated density of 1.7×10^{11} cm^{-2} inside the junction, the Fermi wavelength is about 60 nm, which means we have 133 transport modes in a 4-micron-long junction. This places us at an interface transparency $|t|^2$ of about 98.5%. Realistically, the doping from the aluminum leads could modify the chemical potential inside the junction, and hence the transparency is slightly lower than this number. For example, if we assumed a density of 4.0×10^{11} cm^{-2}, we would find a transparency of 78.4%. Given the uncertainty in our density estimate, we expect our interface transparency to fall inside this range of 78% to 100%.

To investigate the spectrum at the end of the Josephson junction, we perform local tunneling spectroscopy through a weakly coupled electrode, which overlaps the junction over an area of approximately 100 nm by 100 nm near its edge. We use in-situ ion milling to etch most of the CdHgTe barrier layer on top of the quantum well and stop when only a few nanometers of CdHgTe remain. We then deposit 100 nm of gold with 10 nm of titanium as a sticking layer. Both metals, especially the titanium, react chemically with CdHgTe to form alloys[3]. These semimetallic alloys facilitate the tunneling of electrons between the local electrode and the quantum well, producing low-temperature tunnel resistances ranging from 15 kΩ to 15 MΩ, depending on the thickness of the barrier layer and the overlapping area of the electrode with the quantum well.

Since the features in the tunneling conductance we study here are induced by the superconductivity in the aluminum, we expect them to only develop well below the critical temperature of the superconducting aluminum film, which can range from 1.2K to 1.6K [4]. Figure S3 shows the temperature dependence of the tunneling conductance curves during a cool-down process in our dilution refrigerator, for the same device discussed in the main text. As we can see, the main peaks in the conductance only start developing below 0.5 Kelvin. The separation of the two conductance peaks is typically around 120 μeV and the width of each peak is on the order of 50 μeV in energy. Above this temperature, the tunneling conductance curve is mostly flat for this energy range. Although this does not completely rule out all possible contributions from features related to the tunnel probe that only develop at low temperatures, it does strongly suggest that these conductance peaks originate from the aluminum-induced superconducting gap in the HgTe quantum well.

During our measurements, the point in bias voltage about which the conductance curve is approximately symmetric is constant for each cool-down of the device, and we identify this point as the zero-bias point. It is worth pointing out that this true zero-bias point tends to be offset by 15-25 μeV from zero reading on our DC voltage supply, which we attribute to a constant voltage offset that comes from the voltage source in our measurement circuitry which supplies the bias to the tunnel probe. This is a very common experimental feature, where the applied zero voltage does not translate to really zero voltage between the tunnel probe and the sample because electronic components may exert finite bias due to various circuit artifacts. To eliminate this artifact and thus avoid unnecessary confusion for the readers, we have shifted the x-axis in all of our tunneling conductance plots, so that the true zero-bias point algins with the zero-bias reading in the plots. Therefore, the presented plots are relative to the true voltage bias rather than the instrumental reading that contains a systematic error.

2 Correction for Imperfect Sample-Magnet Alignment

Due to imperfect sample-magnet alignment, the in-plane field B_x will generate a small perpendicular component B_z, which offsets the B_z field corresponding to zero-flux in the phase loop. To correct for this effect and maintain our measurement in a range of phase difference near zero, we scan over a range of B_z at each B_x field and identify a range with maximal oscillation amplitude in the tunneling conductance.

Shown in Figure S2a is the conductance in the range of a few mT in B_z near zero, featuring

periodic oscillations as the junction's phase difference is modulated, which gradually dampens as the B_z increases in both positive and negative directions. Based on this experimental observation, we maintain our measurements in the vicinity of zero phase difference by scanning over a range in B_z at each B_x field and selecting a region with maximal oscillations in the tunneling conductance (Figure S2a and b). As the in-plane field B_x increases, this optimal range drifts towards higher B_z values, following a linear dependence to first order (Figures S2c-f).

The phase smearing effect is yet another high-field effect that is not compensated by this correction. Because of the microscopic roughness along the edge of the superconducting electrodes during the sample fabrication, the high in-plane magnetic fields can generate non-uniformity along the normal-superconducting interface, which in turn causes the phase difference along the x-direction of the junction to disperse[2]. This creates a smearing effect on the observed spectroscopy's dependence on phase, reducing the signal-to-noise ratio of the tunneling conductance. Because this effect worsens at high in-plane fields, it is necessary to adopt a junction geometry where the topological phase transition happens at low enough fields before the phase smearing effect masks the experimental signal entirely. In our experiment, the 600nm junction places us in this situation and enables us to see the emergence of the zero-bias peaks associated with the phase transition. Future development to improve the lithography and film quality of the superconducting contacts could help reduce such phase smearing effect and enhance the measurement resolution in both energy and phase at high in-plane fields.

3 The Electron-Hole Asymmetry with In-Plane Field

At zero in-plane field, we generally see a symmetric differential conductance between positive and negative DC voltages, endorsing the particle-hole symmetry in the local spectrum of Andreev bound states (see Main Text Figure 2a as an example). However, such symmetry in the LDOS is not present at high in-plane magnetic fields. This is reflected by an asymmetry in the differential conductance about zero bias voltage[1], which grows with the in-plane magnetic field applied. Figures S4 and S5 show the raw data with this asymmetry at various magnetic fields.

To visualize this asymmetry in the tunneling conductance and see how it develops with the magnetic field, we can average the differential conductance over an entire period in the phase difference, at each in-plane field, as plotted in Figure S7. Furthermore, we can quantify it with the slope of a linear fit to the averaged conductance curve. Shown in Figure S8, the slope representing the asymmetry grows linearly with the magnitude of the in-plane field, and the sign of the asymmetry does not depend on the direction of the field. This is also evident from Figure S6, which shows a continuous evolution as the in-plane field is ramped across a broad range, as well as a broader range in the bias voltage. The out-of-plane component of the B_x field is passively compensated in linear proportion but not perfectly canceled. As a result of the minute remaining B_z field, the zero-bias conductance shows oscillations in the B_x field. We can see the same asymmetry develops from positive to negative B_x fields, although its extent does vary from device to device.

[1] As mentioned in Supplementary Section 1, this true zero bias can be offset from 0 voltage reading by a constant deviation ranging from 15 to 25 μeV, due to instrumental errors.

The exact mechanism for controlling this asymmetry is not well understood and hence remains an interesting topic for further studies. Meanwhile, we can correct for this asymmetry, post-measurement, by averaging the differential conductances at each positive energy with its negative counterpoint and assigning this same value for both points. We perform this symmetrization procedure for each differential conductance trace at all phases and all fields, and the corrected results are shown in Figures 2 and 3 of the main text.

4 Obtaining the Zero-Bias Curvature

To illustrate the continuous opening of the window containing the zero-energy peaks, we analyze the symmetrized data and identify whether the differential conductance curve at each particular B_z and B_x contains a zero-energy peak. To quantify this property, we extract the local curvature of the differential conductance near zero-energy. For any differential conductance curve, we fit a parabola to its central segment, and hence extract the curvature from the fitting parameters. This is a good proxy for whether it contains a zero-energy peak as such peaks would make the center of the otherwise convex part of the curve concave, resulting in a negative curvature.

We obtain the curvature of the zero-energy conductance peak using parabolic fits. As seen in the fitting examples in Figure S9, the sign of the curvature correlates well with whether the curve contains a peak (panels e and f) or dip (panels a and c) at zero energy, and the amplitude roughly indicates its visibility. We can do this for each differential conductance curve at any particular phase difference ϕ and any in-plane field, B_x. The parabolic fit works the worst when

the differential conductance is flat in the central region, as shown in panels b and d. In such cases, our method produces a rather small curvature, so the overall analysis is minimally affected. A colour map of the extracted curvature as a function of both phase difference ϕ and the Zeeman field B_x is shown in Figure 3i of the main text.

We would like to emphasize that the zero-bias curvature, which indicates the presence of a zero-bias peak in the tunneling conductance and is central to our main result, does not change during the symmetrizing process, as can be seen in the examples shown in Figure S10a-c. This is because by symmetrizing the conductance as a continuous function of tunneling voltage, we preserve all even terms in its polynomial expansion and eliminate all odd terms. This results in no error in the fitting coefficient of the second-order term, which is the curvature we extract using the parabolic fit. To provide an intuitive picture, a few examples of the parabolic fits on both raw and symmetrized data are shown in Figure S10a-c. The curvature extracted from symmetrized data is shown in Figure S10d, which shows the same result as extracted from the raw data, which we choose to present in Figure 3i of the main text.

5 Two Additional Devices with Similar Behavior

To demonstrate reproducibility for the general trend of the zero-bias curvature, here we present two other devices with different geometries but showing similar effects as the device shown in the main text. Device Kappa has a junction that is 400nm wide and 4 μm long, with a tunnel resistance around 12 MΩ. The raw and symmetrized conductance data of Device Kappa are shown in Figures

S11 and S12 respectively. Device Zeta has a junction that is 800nm wide and 1 μm long, with a tunnel resistance around 3 MΩ. The raw and symmetrized conductance data of device Zeta are shown in Figures S13 and S14 respectively. Due to their low tunnel conductances, they give low signal-to-noise ratios, making them less immune to the phase smearing effects at high in-plane fields, as discussed in supplementary Section 2. Nevertheless, we see the same qualitative trend of an enhanced zero-energy conductance extending over a growing range of ϕ as the in-plane field increases.

We see again that the electron-hole asymmetry in the tunneling conductance is present in these two devices, and the slopes of this asymmetry in these two devices are opposite to that of the device discussed in the main text. Yet, just like in the case of the device shown in the main text, the sign of this slope is independent of the sign of the field. This suggests the asymmetry may be related to device-specific effects such as local potentials or disorders.

Moving towards narrower junctions brings potential benefits to the experiment. As we will show in Supplementary Section 10, a long junction which is 400nm wide holds the promise of showing zero-bias peaks both associated with the phase transition, in the field range we have measured, and from the Majorana bound states, at even higher fields. However, due to the phase smearing effect, the modulation of our tunneling conductance diminishes much below the field required to see the latter ZBP in this 400-nm-wide junction, and, therefore, we only observe the former type of peak in conductance. This points out an immediate direction for fabrication development to improve the lithographic definition and interfacial quality of the superconducting film

with the quantum well, so that future experiments can go up to higher in-plane fields, and, therefore, down to narrower junctions. Such improvements will allow us to explore this topological phase transition physics and the associated Majorana bound states with a more discrete spectrum, without losing the experimental signal due to the undesired phase smearing effect.

6 Numerical Calculation of the Tunneling Conductance

Our theoretical description of the system is based on the model used in Reference 5 for a two-dimensional semiconductor with Rashba spin-orbit interaction defined on a rectangular region. The region has length L and is divided into three segments: a normal region of width W between two superconducting regions of width W_{SC} (see rectangle with black contour in Figure S15). The Bogoliubov-de Gennes Hamiltonian can be written in the Nambu basis $(\psi_\uparrow, \psi_\downarrow, \psi_\downarrow^\dagger, -\psi_\uparrow^\dagger)$ as $H = \int d^2r \psi^\dagger(\mathbf{r})\mathcal{H}(\mathbf{r})\psi(\mathbf{r})$ with

$$\mathcal{H}(\mathbf{r}) = \Big[\frac{p^2}{2m} - \mu(y) + \frac{m\alpha^2}{2}\Big]\tau_z + E_Z(y)\sigma_x + \alpha(p_x\sigma_y - p_y\sigma_x)\tau_z + \Delta(y)\tau_+ + \Delta(y)\tau_-, \quad (1)$$

where m is the effective mass, α the strength of the Rashba spin-orbit interaction and the σ (τ) are Pauli matrices in spin (particle-hole) space.

The Zeeman energy $E_Z(y) = g(y)\mu_B B/2$, chemical potential μ and pairing strength Δ are all affected by the proximity coupling between the semiconductor and the superconductor and

therefore assume different values in the junction and in the leads. We write

$$\Delta(y) = \Delta[e^{-i\phi/2}\Theta(-y) + e^{i\phi/2}\Theta(y-W)], \tag{2}$$

$$g(y) = g_N\Theta(y)\Theta(W-y) + g_{SC}[1-\Theta(y)\Theta(W-y)], \tag{3}$$

$$\mu(y) = \mu_N\Theta(y)\Theta(W-y) + \mu_{SC}[1-\Theta(y)\Theta(W-y)], \tag{4}$$

where ϕ is the phase difference across the junction. Because of the experimental finding that the coherence peaks remain at the same energy for the entire magnetic field range, we henceforth assume the Zeeman energy to be completely suppressed in the superconducting part setting $g_{SC} = 0$ and denote $E_Z = g_N\mu_B B/2$.

For the numerical calculations it is convenient to consider the same model on a square lattice. The corresponding tight-binding Hamiltonian can be written in terms of the Nambu spinors $c_{i,j} = (c_{i,j,\uparrow}, c_{i,j,\downarrow}, c^\dagger_{i,j,\downarrow}, -c^\dagger_{i,j,\uparrow})^{\mathrm{T}}$ as

$$\begin{aligned} H = &-\sum_{i=1}^{L-1}\sum_{j=-W_{SC}+1}^{W+W_{SC}} [c^\dagger_{i,j}(t + i\alpha_{\mathrm{TB}}\sigma_y)\tau_z c_{i+1,j} + \mathrm{h.c.}] \\ &-\sum_{i=1}^{L}\sum_{j=-W_{SC}+1}^{W+W_{SC}-1} [c^\dagger_{i,j}(t - i\alpha_{\mathrm{TB}}\sigma_x)\tau_z c_{i,j+1} + \mathrm{h.c.}] \\ &+\sum_{i=1}^{L}\sum_{j=-W_{SC}+1}^{W+W_{SC}} \Big[c^\dagger_{i,j}\Big(4t + \frac{\alpha^2_{\mathrm{TB}}}{t} - \mu(j) + E_Z(j)\sigma_x\Big)\tau_z c_{i,j} + (\Delta(j)c_{i,j}\tau_x c_{i,j} + \mathrm{h.c.})\Big] \end{aligned} \tag{5}$$

In the limit $t \to \infty$, the tight-binding model maps onto the continuum model in Eq. (1) with the replacements $c_{i,j} \to a\psi(\mathbf{r})$, $\alpha_{\mathrm{TB}} \to \alpha/2a$ and $t \to 1/2ma^2$, where a is the lattice constant.

For the numerical calculations presented in the main text, we use the following parameters in the continuum model of Eq. (1): $\alpha = 34\,\mathrm{meVnm}$, $\Delta = 64\,\mu\mathrm{eV}$, $\mu_N = 12.5\,\mathrm{meV}$, $\mu_{SC} = 50\,\mathrm{meV}$,

$g_n = 10$, and $m = 0.033m_e$, where m_e is the electron mass.

The tight-binding parameters are chosen accordingly as $t = 32\,\text{meV}$, $\alpha_{\text{TB}} = 0.089t$, and $a = 6\,\text{nm}$.

The phase diagram and subgap spectrum shown in Figure 1 of the main text is evaluated using the continuum model with $L = \infty$ and $W_{SC} = \infty$. In this case the momentum along the x direction is conserved and can be replaced by a number k_x. The subgap spectrum can then be found by evaluating the scattering matrix $S(E)$ for states inside the junction and solving the equation

$$\det\{1 - S[E(k_x)]\} = 0 \tag{6}$$

(see Reference 5 for the numerical procedure). The phase boundaries correspond to zero-energy crossings at $k_x = 0$.

An evaluation of the conductance through the system requires the addition of external leads. To model the experimental setup, we attach a normal lead near the upper edge of the normal region and two superconducting leads contacting the lower edges of the superconducting segments as shown in Figure S15. We choose system dimensions $L = 150$, $W = 100$, and $W_{SC} = 200$ corresponding to a junction area of $900\,\text{nm} \times 600\,\text{nm}$.

The normal lead is added as a second layer, which extends infinitely in the $x \to -\infty$ direction and is connected to the junction by vertical tunnel couplings in the area $i_1 \leq i \leq i_2$ and $j_1 \leq j \leq$

j_2. The additional contribution to the Hamiltonian reads

$$H_L = \sum_{i=-\infty}^{i_2}\sum_{j=j_1}^{j_2}(4t-\mu_L)d^\dagger_{i,j}\tau_z d_{i,j} \\ -\Big(t\sum_{i=-\infty}^{i_2-1}\sum_{j=j_1}^{j_2} d^\dagger_{i,j}\tau_z d_{i,j+1} + t\sum_{i=-\infty}^{i_2}\sum_{j=j_1}^{j_2} d^\dagger_{i-1,j}\tau_z d_{i,j} + t_L\sum_{i=i_1}^{i_2}\sum_{j=j_1}^{j_2} d^\dagger_{i,j}\tau_z c_{ij} + \text{h.c.}\Big) \quad (7)$$

In our simulations, we choose $\mu_L = 4t$, $t_L = 0.2t$. The contact area is defined by $i_1 = 1$, $i_2 = 6$, $j_1 = 43$, $j_2 = 58$, which corresponds to an area of $\sim 40\,\text{nm} \times 100\,\text{nm}$.

The superconducting leads simply continue the two superconducting segments in the $x \to \infty$ direction

$$H_{SC,L} = -\sum_{i=L+1}^{\infty}\Big(\sum_{j=-W_{SC}+1}^{0} + \sum_{j=W+1}^{W+W_{SC}}\Big)\Big[\Big(4t + \frac{\alpha_{\text{TB}}^2}{t} - \mu_{SC}\Big)c^\dagger_{i,j}\tau_z c_{i,j} + (\Delta(j)c_{i,j}\tau_x c_{i,j} + \text{h.c.})\Big] \\ -\sum_{i=L}^{\infty}\Big(\sum_{j=-W_{SC}+1}^{0} + \sum_{j=W+1}^{W+W_{SC}}\Big)[c^\dagger_{i,j}(t + i\alpha_{\text{TB}}\sigma_y)\tau_z c_{i+1,j} + \text{h.c.}] \\ -\sum_{i=L}^{\infty}\Big(\sum_{j=-W_{SC}+1}^{-1} + \sum_{j=W+1}^{W+W_{SC}-1}\Big)[c^\dagger_{i,j}(t - i\alpha_{\text{TB}}\sigma_x)\tau_z c_{i,j+1} + \text{h.c.}]. \quad (8)$$

We use the KWANT library to calculate the scattering matrix of the system with respect to the external leads. The conductance between the normal lead at a finite bias voltage eV and the two grounded superconductors can then be evaluated according to the formula

$$G(eV) = \frac{e^2}{h}[N - R_{ee}(eV) + R_{eh}(eV)], \quad (9)$$

where N is the number of channels in the lead and $R_{ee,eh}(\epsilon)$ are the normal and Andreev reflection probability in the normal lead at energy ϵ. To account for the limited energy resolution in the

experiment, we convolute the conductance as a function of energy with a Gaussian with standard deviation $24\,\mu$eV. Moreover, we include a broadening of the conductance as a function of phase difference by convolution with a Gaussian with standard deviation 0.4π. This accounts for an inhomogeneous phase difference across the junction in the experiment, caused by the flux threaded through the junction area and a spatially varying random phase due to the combination of the parallel field and the interface roughness of the superconducting leads[2].

7 Majorana Wavefunction

To elucidate possible Majorana signatures in the conductance, we calculate the local density of states (LDOS) associated with the lowest energy state in the junction. A bona-fide Majorana state only exists in a semi-infinite system. To consider this situation, we set $L \to \infty$ in the setup in Figure S15, such that both superconducting leads and the normal region are semi-infinite. We can then calculate the LDOS at zero energy as a function of position using KWANT.

The resulting spectra weight of the Majorana state is shown in Figure S16(a). While the state is indeed localized at the edge, its decay is nonexponential. This is consistent with the fact that the coherence length is very long for the parameters assumed in the previous section. The typical scale for the induced gap is $1/mW^2 \simeq 6\,\mu$eV which agrees with our numerical calculations of the energy spectrum. This gap translates into a coherence length of $\sim 45\mu m$.

We can also calculate the LDOS in finite-length junctions using the setup in Figure S15. In this case, the Majorana states at the two ends hybridize and form a finite energy excitation. In

Figure S16(b) and (c), we show the LDOS corresponding to the lowest energy state for $L = 6\,\mu$m and $L = 900\,$nm. In Figure S16(b), the edge localization remains visible. In contrast, the $900\,$nm junction in Figure S16(c) is too short to allow for any distinction between edge and bulk and the lowest-energy state is homogeneously distributed along the entire length of the junction.

These results suggest that, even though the system is in the topological phase, signatures of Majorana states cannot be distinguished from bulk signatures in devices with current dimensions.

8 Origin of the Zero-Bias Conductance Peak

The normal probe in the experiment is in the tunneling regime and the conductance is therefore expected to reflect the local density of states in the junctions. The long Majorana localization length discussed above implies a weak contribution of Majoranas to the conductance, which is washed out due to the energy broadening. Instead, the subgap conductance will be dominated by the band of Andreev states that extend along the entire length of the junction.

In this section, we derive an analytical formula for the Andreev spectrum in a certain limiting case, which can be compared with the numerical results for the full Hamiltonian (1) shown in Figure 1e of the main text. We then use this estimate to calculate the density of states.

To gain analytical insight, we assume that edge effects are small and simply consider the bulk density of states in an infinitely long junction, in which the momentum component k_x is conserved. We first focus on the case of perfect Andreev reflection and later include normal reflection. As

previously, we determine the bound state energies E as a function of k_x from the scattering matrix equation (6) within the continuum model Eq. (1). It is expedient to introduce the polar angles θ_i defined by $\cos\theta_i = k_x/k_{F,i}$, where $i = 1, 2$ denotes the two Fermi surfaces and $k_{F,1/2} = \sqrt{2m\mu} \pm m\alpha$.

We can further simplify Eq. (6) in the case that Andreev reflection does not mix the two Fermi surfaces. This is strictly true only at $k_x = 0$, where the spins on the two Fermi surfaces are antiparallel, while at nonzero k_x, a right moving electron can be Andreev reflected into a superposition of left moving holes from both Fermi surface sheets due to a nonzero overlap of spin states[5].

In the limit $E_Z, \Delta \ll \alpha k_F$, however, the two spins along a particular momentum direction are antiparallel because of the Rashba-induced spin-momentum locking. In this case, the two Fermi surfaces at a fixed k_x have approximately opposite spins as long as the corresponding polar angles have similar magnitude $\theta_1(k_x) \simeq \theta_2(k_x) \equiv \theta(k_x)$.

Under these conditions, Eq. (6) yields[5]

$$\arccos\Big[\frac{E(k_x)}{\Delta}\Big] = \frac{\pi}{2}\frac{E(k_x)}{E_T(k_x)} - \frac{\pi}{2}\frac{\sin\theta E_Z}{E_T(k_x)} \pm \frac{\phi}{2} + n\pi, \qquad n \in \mathbf{Z}, \tag{10}$$

where $E_T(k_x) = (\pi/2)\sin\theta v_F/W$ is the Thouless energy. The angular dependence of $E_T(k_x)$ reflects the longer distance between the superconducting leads for wavepackets with oblique incidence. The factor $\sin\theta E_Z$ accounts for the fact that spins rotate along the Fermi surface. Considering the limit $E_T(k_x) \gg \Delta$ as is appropriate in our parameter regime for states near $k_x = 0$

[$E_T(k_x = 0) = 630\,\mu$eV], we find

$$E = \Delta \cos\Big(\frac{W E_Z}{v_F} \pm \frac{\phi}{2} + n\pi\Big) \tag{11}$$

which is independent of k_x. Hence the bands are expected to be relatively flat. As k_x approaches the Fermi momentum, $E_T(k_x)$ decreases and the energy becomes momentum dependent. This is behavior is consistent with the spectrum in Figure 1e of the main text. We caution, however, that Eq. (10) requires $\theta_1 \simeq \theta_2$ and therefore ceases to be valid as k_x approaches the Fermi momenta.

The flatness of the dispersion should result in a strong peak in the LDOS at the corresponding energy, while the spectral weight at other energies is smaller. This implies that topological phase transitions, where the energy in Eq. (11) vanishes, are signaled by a conductance peak at zero bias. Importantly this is a feature of the bulk density of states and does not take into account the contribution of the Majorana states.

The spectrum changes when normal reflection is taken into account. We specifically consider normal reflection from the superconducting leads that conserves the momentum along the x direction, e.g., caused by a potential step at the N-S interface. In this case, we have to modify Eq. (10) by replacing

$$\phi \to \tilde{\phi} = \arccos[r^2 \cos(2 \sin\theta k_F W + 2\varphi_N) + (1 - r^2)\cos\phi], \tag{12}$$

where r is the normal reflection amplitude and φ_N is a phase shift associated with the normal reflection that depends on microscopic details. Details of the derivation can be found in Reference 5 (the prefactor $\sin\theta$ was missing in the reference). Since for our choice of parameters we have

$k_F W \gg 1$, the first term in the square brackets above oscillates rapidly as a function of k_x. This results in oscillation of the Andreev energy as a function of k_x with an amplitude that scales with the reflection probability.

Indeed, these oscillations also occur in the numerical spectra shown in Figure 1f of the main text.

Since normal reflection broadens the band of Andreev states, the density of states calculated from Eqs. (11) and (12) exhibits significant contributions over a range of energy values. This can be seen in Figure S17, which shows the density of states for various values of the in-plane magnetic field calculated using Eqs. (11) and (12).

There are two van Hove singularities at the band edges because all maxima and minima of $E(k_x)$ in Eq. (11) occur at the same energies.

The band center and the approximate band width in Figure S17a is consistent with the numerical spectra shown in Figure 1e of the main text. Moreover, for $B = 0\,\mathrm{T}$ and $1.6\,\mathrm{T}$ the energy minima and maxima of the spectra are roughly aligned for not too large momenta in agreement with our analytical findings. The spectrum at $B = 1\,\mathrm{T}$, in contrast, has aligned minima but not maxima.

By varying either ϕ or E_Z, one can tune the band center across zero energy. Once the band crosses zero energy the positive and negative energy band overlap which leads to an enhanced

density of states at zero energy. For weak normal reflection, the band widths are small and the density of states shown in Figure S17a is enhanced near zero energy only in a narrow window around the phase transition. This behavior is consistent with the spectra shown in Figure 1e of the main text.

If the normal reflection is higher, the band width increases as shown in Figure S17b. In this case, the density of states is enhanced near zero energy in a larger range of magnetic fields. While the density of states does not typically have a maximum at zero, an additional energy broadening applied to the data may result in a zero-bias peak. If the broadening is sufficiently large, the peak can persist between $B = 0.8\,\mathrm{T}$ and $B = 1.2\,\mathrm{T}$ for the parameters of Figure S17b. Such a behavior is quantitatively consistent with the numerical data for the conductance in Figure 4g of the main text, which shows a peak at zero bias over an extended region in parameter space.

We conclude that a zero-bias peak in the conductance signals the zero-energy crossing of a band of Andreev states, which corresponds to a topological phase transition. The width of the band is determined by the normal reflection probability from the superconducting leads. In the presence of a nonzero band width and an additional broadening of the data in energy, a zero-bias peak can occur over an extended range of magnetic field strengths and phase differences in agreement with the experimental observations as well as the numerical results presented in the main text.

9 Finite-Difference Scheme and Exact Diagonalization

To show that the peak in the $\mathrm{d}I/\mathrm{d}V$ characteristics at the topological transition is a universal property for wide junctions, while for narrower junctions a competition between Andreev and Majorana bound states occurs, we perform a second type of calculations. Complementary to the previous section, we employ a finite-difference scheme to obtain the eigenspectrum and eigenstates of the finite Josephson junction shown in Figure S18. These eigenstates and eigenenergies are then used to compute the local density of states (LDOS) at the edge of the normal region. For this purpose, we use the Hamiltonian (Eq. 1-4) and invoke hard-wall boundary conditions in x- and y-directions to describe a Josephson junction of finite length L in x-direction and finite width $W_{tot} = W + 2W_{SC}$ in y-direction. Here, W is the width of the normal region and W_{SC} denotes the finite widths of the superconducting regions (see Figure S18). We discretize the Hamiltonian (Eq. 1-4) using $\mathrm{d}\psi(x)/\mathrm{d}x \to [\psi(x_i+a)-\psi(x_i-a)]/2a$, $\mathrm{d}^2\psi(x)/\mathrm{d}x^2 \to [\psi(x_i+a)-2\psi(x_i)+\psi(x_i-a)]/a^2$, and analogous expressions for the derivatives with respect to y, where a and $x_i = ai$ (with $i \in \mathbb{Z}$) denote the discrete step size and lattice sites, respectively. This procedure yields Eq. 5. If Eq. 5 is written in the form

$$H = \sum_{i,i'=1}^{L} \sum_{j,j'=-W_{SC}+1}^{W+W_{SC}} \mathcal{H}_{i,j;i',j'}\, c^{\dagger}_{i,j} c_{i',j'}, \tag{13}$$

the eigenenergies $E^{(n)}$ and eigenstates $c^{(n)}_{i,j}$ of the system are found by diagonalizing the eigenvalue equation

$$\sum_{i'=1}^{L} \sum_{j'=-W_{SC}+1}^{W+W_{SC}} \mathcal{H}_{i,j;i',j'}\, c^{(n)}_{i',j'} = E^{(n)} c^{(n)}_{i,j}, \tag{14}$$

where n denotes the n-th eigenstate.

These eigenenergies and eigenstates are then used to compute the LDOS at the upper edge of the normal region as a function of energy E,

$$\mathrm{LDOS}(E) = \sum_{i=1}^{l_x} \sum_{j=W/2-l_y/2}^{W/2+l_y/2} \sum_{n} \left| c_{i,j}^{(n)} \right| \delta_\Gamma(E - E^{(n)}). \tag{15}$$

Here, $\delta_\Gamma(E - E^{(n)})$ is modeled by a Gaussian with broadening Γ. The area of summation is chosen to resemble the area covered by the tunneling probe with lengths l_x and l_y in x- and y-directions, respectively (see Figure S18). In the lowest-order approximation, the $\mathrm{d}I/\mathrm{d}V$ characteristic is proportional to the LDOS. Hence, to compare with the experiment and the KWANT simulations, we first compute the LDOS for a given probe area and position and then look at the curvature $\partial^2 \mathrm{LDOS}/\partial E^2$ around $E = 0$.

10 Comparison of the Local Density of States for Josephson Junctions with Different Widths

In general, a zero-energy peak in the edge LDOS can originate from Majorana end states and/or low-energy bulk Andreev bound states. As discussed in the main text, the most pronounced zero-energy peaks for a 600nm wide junction are expected to actually arise from the bulk Andreev bound states that describe the topological phase boundaries. Here, we study and compare the coexistence of zero-energy peaks in the edge LDOS due to Majorana end states and bulk Andreev states for samples of width $W = 600$ nm and $W = 400$ nm.

For the calculations with a $W = 600$ nm wide normal region, we have used α=16 meVnm,

Δ=65 μeV, $\mu_N = 12.5$ meV, $\mu_{SC} = 25$ meV, $g_N = 10$, $g_{SC} = 0$, and $m = 0.038m_e$. The size of the superconducting regions is $900\text{nm}\times700\text{nm}$ and the size of the normal region $900\text{nm}\times600$ nm in x- and y-directions, with a probe size of $100\text{nm}\times100\text{nm}$. The discretization step is chosen as $a = 10$ nm. The lengths and widths as well as their corresponding numbers of steps are described by the same quantities, i.e. $L = 90$, $W_{tot} = 200$, $W_{SC} = 70$, $W = 60$, $l_x = 10$, and $l_y = 10$. To compute the LDOS via Eq. (15), a Gaussian broadening of $\Gamma = 0.25\Delta$ for $\delta_\Gamma(E - E^{(n)})$ has been used.

Figure S19 shows $\partial^2\text{LDOS}/\partial E^2$ at $E = 0$ for the above parameters as a function of the magnetic field B_x and the external phase difference ϕ between the two superconductors. Similar to the experiment and our KWANT simulations, we find that a zero-energy peak ($\partial^2\text{LDOS}/\partial E^2 < 0$) in the LDOS starts to appear at fields around $B_x = 0.4 - 0.5$ T and becomes the most pronounced around $B_x = 1.2$ T. As B_x increases further and (ϕ, B_x) moves away from the boundaries of the topological phase, the zero-bias peak disappears.

We note that we have chosen somewhat different parameters for the superconducting regions here compared to the KWANT simulations: The finite width W_{SC} of the superconducting regions is reduced to 700 nm (compared to 1200 nm), thereby increasing the amount of normal reflection due to the finite size of the superconductors. This effect is somewhat compensated for by reducing the mismatch between the chemical potentials μ_N and μ_{SC} (12.5:25 compared to 12.5:50 in the KWANT calculations), which is a second source for normal reflection at the S/N interfaces.

Likewise, the strength of Rashba SOC in the entire device is reduced by a factor of around 2

to $\alpha = 16$ meVnm to demonstrate the robust occurrence of a zero-energy peak in the LDOS/a zero-bias peak in the $\mathrm{d}I/\mathrm{d}V$-characteristic for a wide range of Rashba SOC strengths. This robustness with Rashba spin-orbit strength α of the topological phase boundaries and of zero-energy peaks at (segments of) these boundaries can also be explained within a scattering matrix approach.

The nature of the Majorana bound state is illustrated in Figure S20, which shows the probability amplitude $|\Psi(x, y)|^2$ of the lowest-energy state at $B_x = 1.2$ T and a phase difference $\phi = \pi$. Due to the finite length L of the setup and the resulting hybridization of the two separate Majorana end states, this state is not situated at zero-energy. As argued above in Supplementary Section 7, due to the small induced topological gap of the order of 6 μeV protecting the Majorana end states, these states are expected to decay only slowly away from the upper and lower edges of the normal region. This feature is exhibited in Figure S20, where the lowest energy state is spread over the entire normal region and only slightly localized at the boundaries of the normal region (see also Figure S16).

The large localization length of the Majorana end states in the sample with a 600-nm-wide normal region implies that the zero-energy peaks in the edge LDOS arise almost entirely from the bulk Andreev bound states at the topological phase boundaries. Indeed, comparing $\partial^2\mathrm{LDOS}/\partial E^2$ around $E = 0$ computed at the edge with that computed in the center of the normal region yields qualitatively similar results.

To obtain more localized Majorana bound states, the topological gap, of the order of $\hbar^2/(mW^2)$, should be increased. Hence, a potential route is decreasing the width W and going to narrower de-

vices. In fact, a sample with a $W = 400$ nm wide normal region is also available, Device Kappa in Supplementary Section 5. Figure S21 shows $\partial^2\mathrm{LDOS}/\partial E^2$ obtained for a junction of width $W = 400$ nm. In Figure S21, the parameters are α=160 meVnm, Δ=130 μeV, $\mu_N = 10$ meV, $\mu_{SC} = 20$ meV, $g_N = 10$, $g_{SC} = 0$, and $m = 0.038m_e$. Here, the size of the superconducting regions is 1000nm$\times 800$nm in x- and y-directions, that of the normal region 1000nm$\times 400$ nm, and that of the probe 100nm$\times 100$nm. Using again a discretization step of $a = 10$ nm, the corresponding numbers of steps are $L = 100$, $W_{tot} = 200$, $W_{SC} = 80$, $W = 40$, $l_x = 10$, and $l_y = 10$ (again these symbols denote widths/lenghts as well as the number of steps). The LDOS is computed with a Gaussian broadening of $\Gamma = 0.2\Delta$ in Eq. (15).

Similarly to Figure S19, the curvature of the LDOS at the edge of the normal region is shown in Figure S21(a). For these parameters, the topological phase arises only for fields above $B_x = 1$ T, as illustrated by the dashed lines denoting the boundaries of the topological phase. These boundaries have been obtained numerically for an infinitely long system ($L \to \infty$), which has otherwise the same parameters as Figure S21(a). Whereas for the edge LDOS, no zero-energy peak is found outside the topological region ($\partial^2\mathrm{LDOS}/\partial E^2 > 0$; red areas in Figure S21), a zero-energy peak of the edge LDOS appears for a wide range of phase differences ϕ inside the topological region ($\partial^2\mathrm{LDOS}/\partial E^2 < 0$; blue areas in Figure S21). This is in contrast to the bulk LDOS measured in the center of the normal region (yellow area in Figure S18): As shown in Figure S21(b), no zero-energy peak develops for the bulk LDOS, apart from a small region in phase space slightly below $B_x = 3$ T and from $\phi \approx 0$ to $\phi \approx 0.4\pi$.

These regions with $\partial^2 \mathrm{LDOS}/\partial E^2 < 0$ in the bulk LDOS arise from Andreev bound states at the phase boundary, providing again a fingerprint of the topological transition. We note that due to the much stronger Rashba SOC chosen here compared to Figure S19, the radii of the two Rashba-split Fermi circles differ considerably. Thus, the Andreev bound states arising mainly from the larger of the two Fermi circles carry significantly more weight in the LDOS than those arising from the smaller Fermi circle. As a consequence, pronounced zero-energy peaks in the bulk LDOS occur primarily at those phase boundaries that correspond to Andreev bound states formed from the larger Fermi circle.

Moreover, Figure S21(b) shows that the phase boundaries are usually traced by regions of nearly zero curvature (white regions), indicative of a flat LDOS at these boundaries. This is consistent with the high normal reflection that is implied by the squeezed topological regime in Figure S21. Indeed, large normal reflection increases the band widths of the Andreev bound states and thus the range of energies over which a flat LDOS can be expected (see Sec. 8). For the energy broadening $\Gamma = 0.2\Delta$ in Figure S21, the LDOS around $E = 0$ remains flat at the phase boundaries.

The above difference between the edge and bulk LDOS points to the zero-/low-energy states being localized at the edge of the normal region. This is indeed corroborated by Figure S22, which, as an example, shows the wave function of the lowest-energy state at $B_x = 2.4$ T and $\phi = 1.8\pi$: Here, the weight of the low-energy wavefunction at the edge of the normal region is significantly higher than the weight in the center of the junction.

The above results imply that for junctions with normal regions of width $W = 400$ nm, it

could be possible to observe signatures of Majorana bound states by comparing the edge and bulk LDOS. Such signatures, however, are expected to occur for magnetic fields beyond the current experimental regime. Still, going to narrower devices with improved fabrication technology offers a promising route for finding fingerprints of Majorana bound states, difficult to isolate in Josephson junctions with wide normal regions.

1. Hart, S. *et al.* Induced superconductivity in the quantum spin Hall edge. *Nature Physics* **10**, 638–643 (2014).

2. Hart, S. *et al.* Controlled finite momentum pairing and spatially varying order parameter in proximitized HgTe quantum wells. *Nature Physics* **13**, 87–93 (2017).

3. Capper, G. *Mercury Cadmium Telluride: Growth, Properties and Applications* (John Wiley & Sons, 2011).

4. Meservey, R. & Tedrow, P. M. Properties of very thin aluminum films. *Journal of Applied Physics* **42**, 51–53 (1971).

5. Pientka, F. *et al.* Topological superconductivity in a planar Josephson junction. *Physical Review X* **7**, 1–17 (2017).

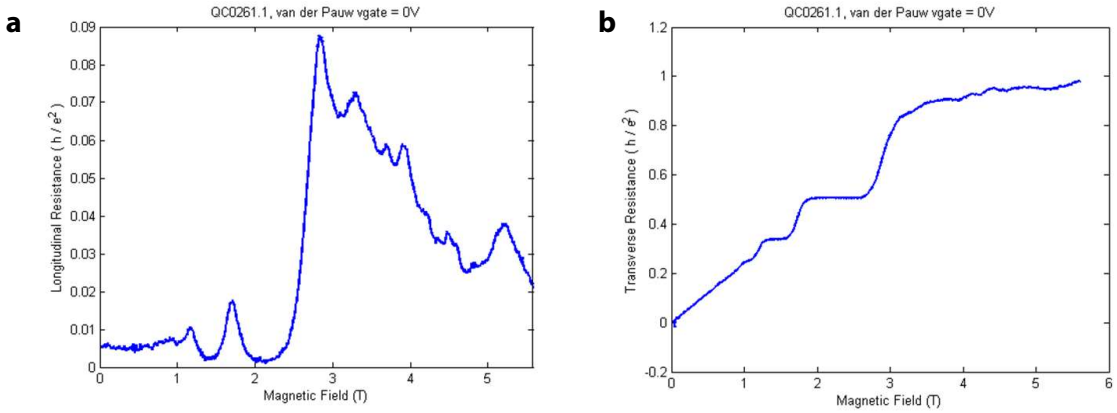

Figure S1 Characterization of the HgTe quantum well. Shown here are the longitudinal and Hall resistances of a van der Pauw device fabricated on wafer QC0261, as a function of the perpendicular magnetic field, at a top gate voltage of 0 V, measured at a temperature of 4 Kelvin.

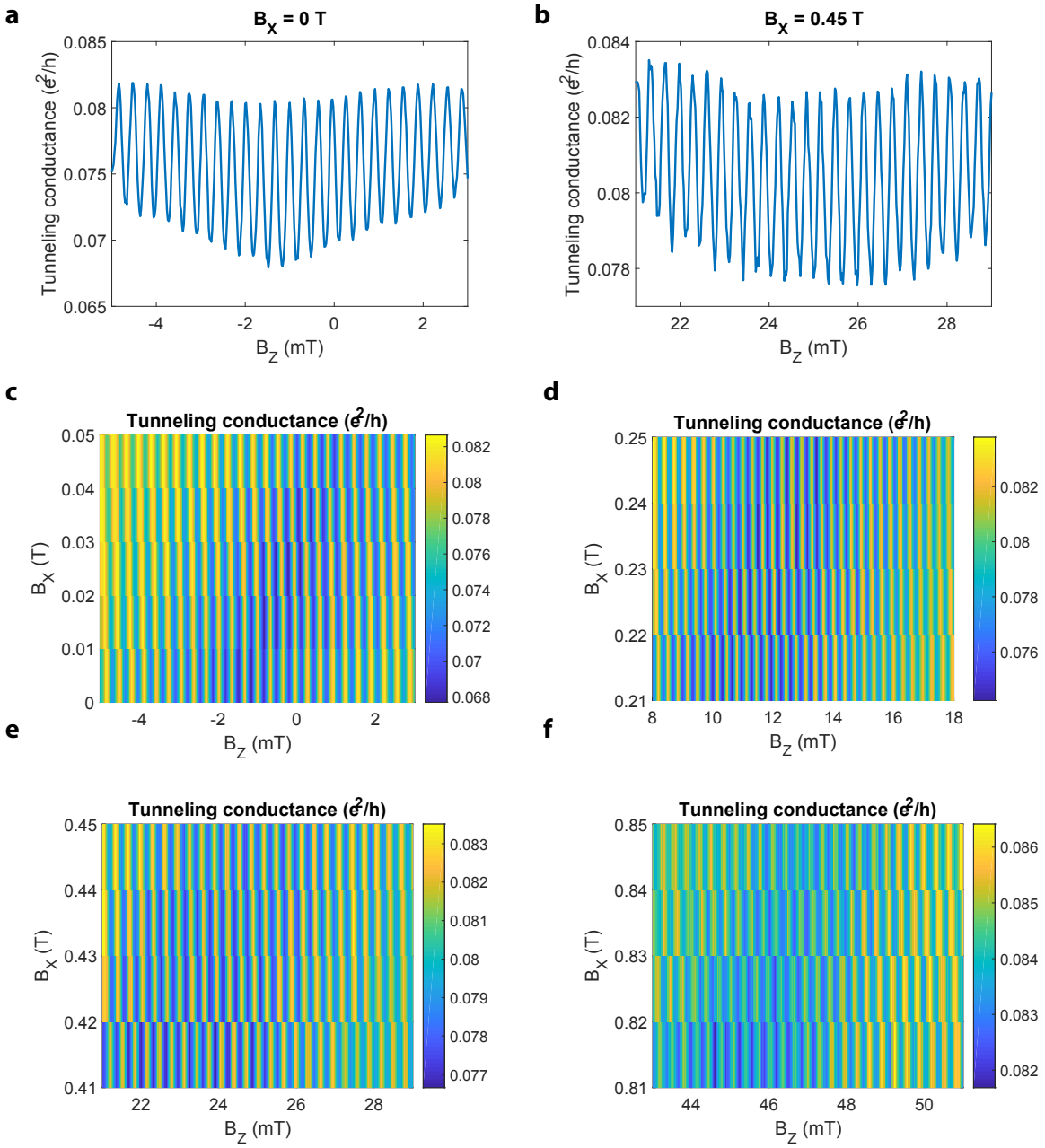

Figure S2 Compensation for the sample-magnet misalignment. a and b, The tunneling conductance near zero bias as a function of the out-of-plane magnetic field, B_z, at zero in-plane field $B_x = 0$ T in a) and a finite in-plane field $B_x = 0.45$ T in b). c-f, Colourplots of tunneling conductance near zero bias as a function of both the out-of-plane magnetic field B_z and the in-plane field B_x. At incremental ranges of B_z, these uncompensated plots show the linear offset of B_z growing with increasing B_x.

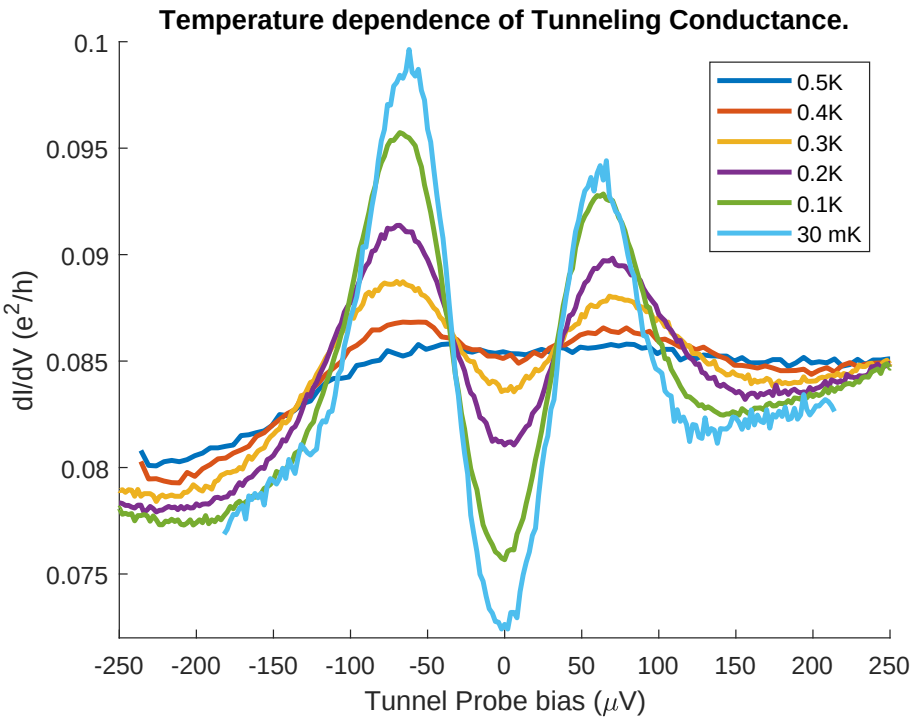

Figure S3 Temperature dependence of the tunneling conductance. Shown here is temperature dependence of the tunneling conductance of the same device as discussed in the main text, plotted against the DC bias across the tunnel probe and the superconducting lead. Different curves represent data taken at different averaged temperatures during its cool-down in our dilution refrigerator, from 0.5 Kelvin (blue curve) down to 31 millikelvins (teal curve) over a range of 0.5 mV of DC bias.

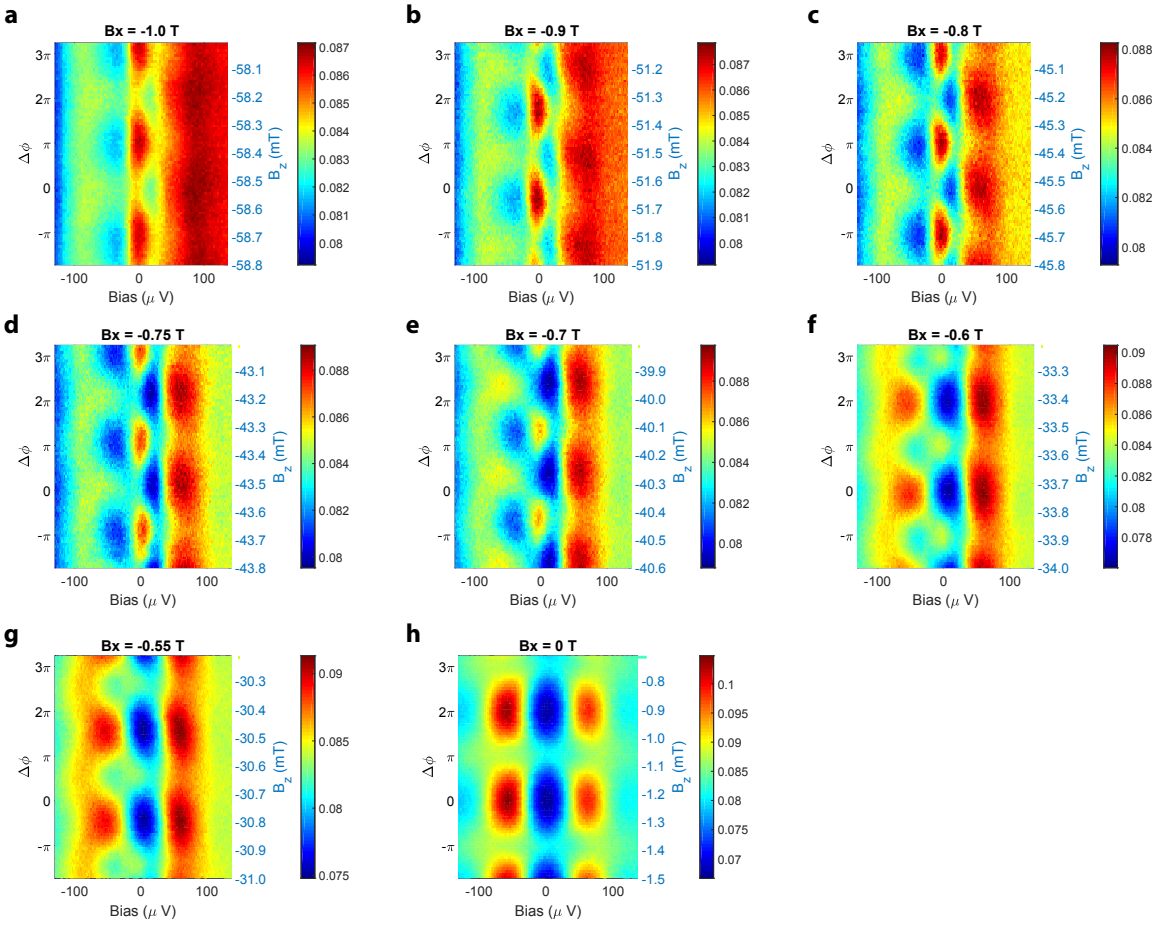

Figure S4 Unprocessed conductance data with in-plane magnetic fields, part 1. The raw conductance data (in units of e^2/h) at in-plane fields ranging from -1.0 T to 0 T, with an electron-hole asymmetry which grows as the magnitude of the in-plane field increase from 0 to 1.0 T. All plots show tunneling conductance in units of e^2/h as a function of both bias voltage and the span over a range of 0.8 mT in B_z.

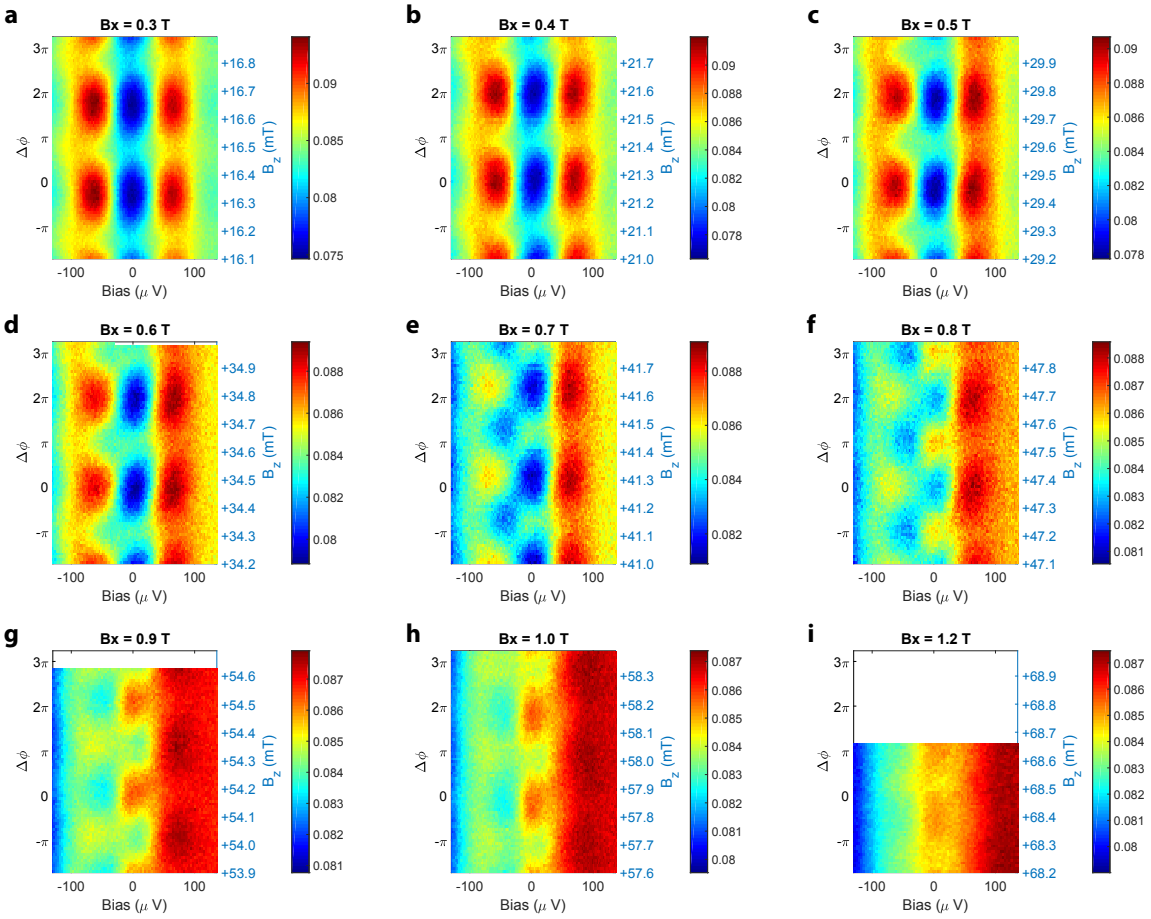

Figure S5 Unprocessed conductance data with in-plane magnetic fields, part 2. The raw conductance data (in units of e^2/h) with an electron-hole asymmetry which grows as the in-plane field increases from 0.3 T to 1.2 T. All plots show tunneling conductance in units of e^2/h as a function of both bias voltage and the span over a range of 0.8 mT in B_z.

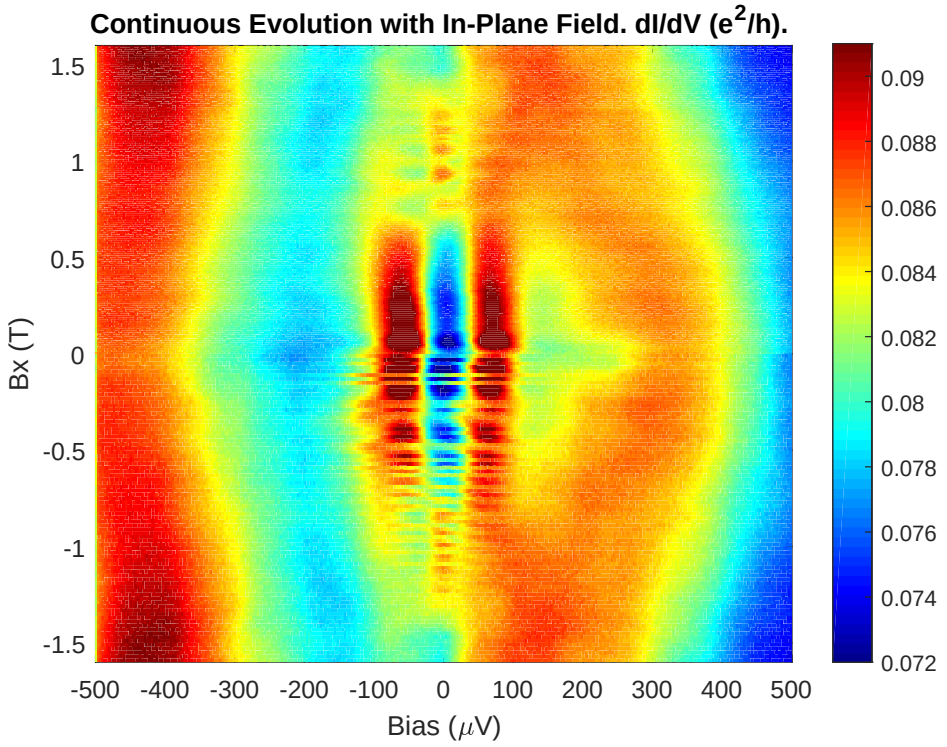

Figure S6 Differential conductance colourmap as B_x varies continuously. Shown here is a continuous evolution of the tunneling conductance curve, over a wide range of the in-plane field B_x from -1.6 T to 1.6 T. Because our compensation of the perpendicular component of the in-plane magnetic field is not perfect, there is still a small flux which causes oscillations in the phase ϕ at the same time as the field grows. Data shown here is obtained from the same device as discussed in the main text.

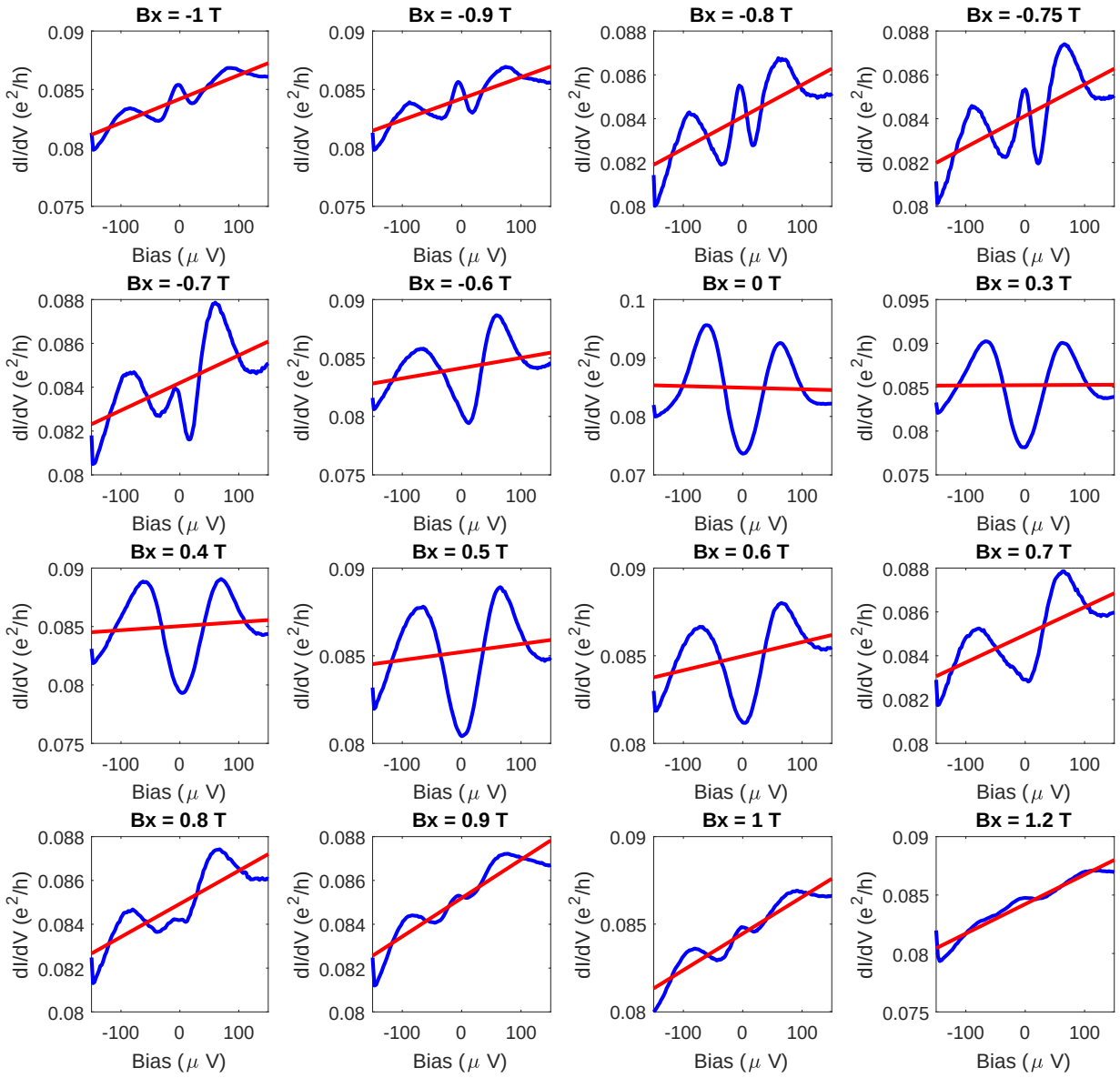

Figure S7 Development of the electron-hole asymmetry with the in-plane field. Each panel above shows, in a blue, solid curve, the raw measurement of the tunneling conductance, averaged over an entire period in the phase difference ϕ, at a given in-plane field B_x, labeled above the panel. The red line in each panel shows the linear regression of that tunneling conductance curve, from which the slope representing the asymmetry is extracted.

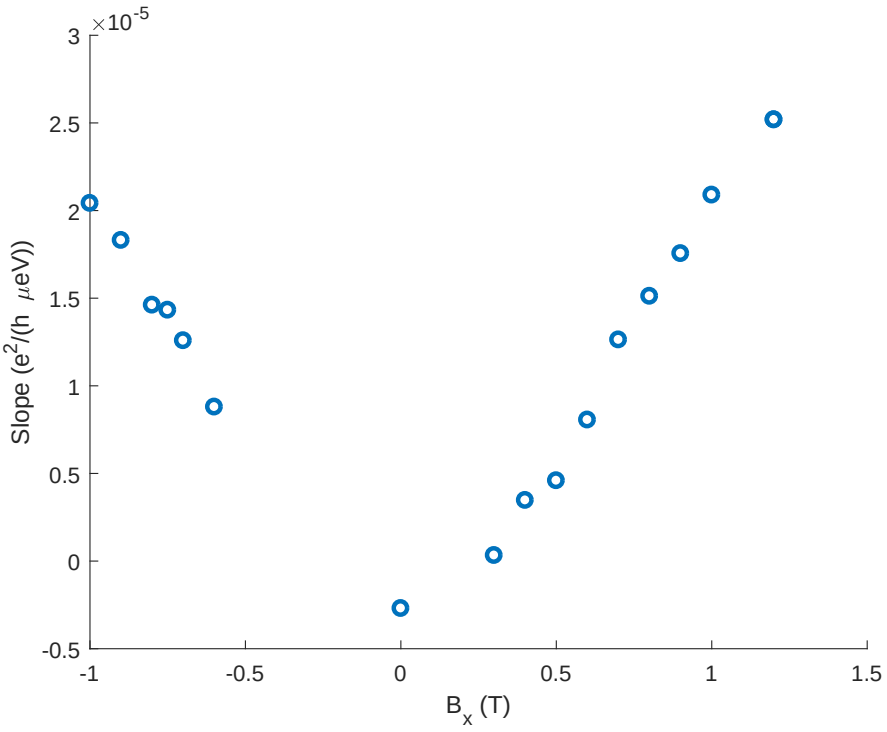

Figure S8 Slope of the electron-hole asymmetry versus the in-plane magnetic field. Each point in the above plot represents a slope extracted from the linear regression shown in Figure S7, in units of $e^2/(h \cdot \mu eV)$. Overall, the asymmetric slope increases linearly with the magnitude of the in-plane field, and it is independent of the sign of the field.

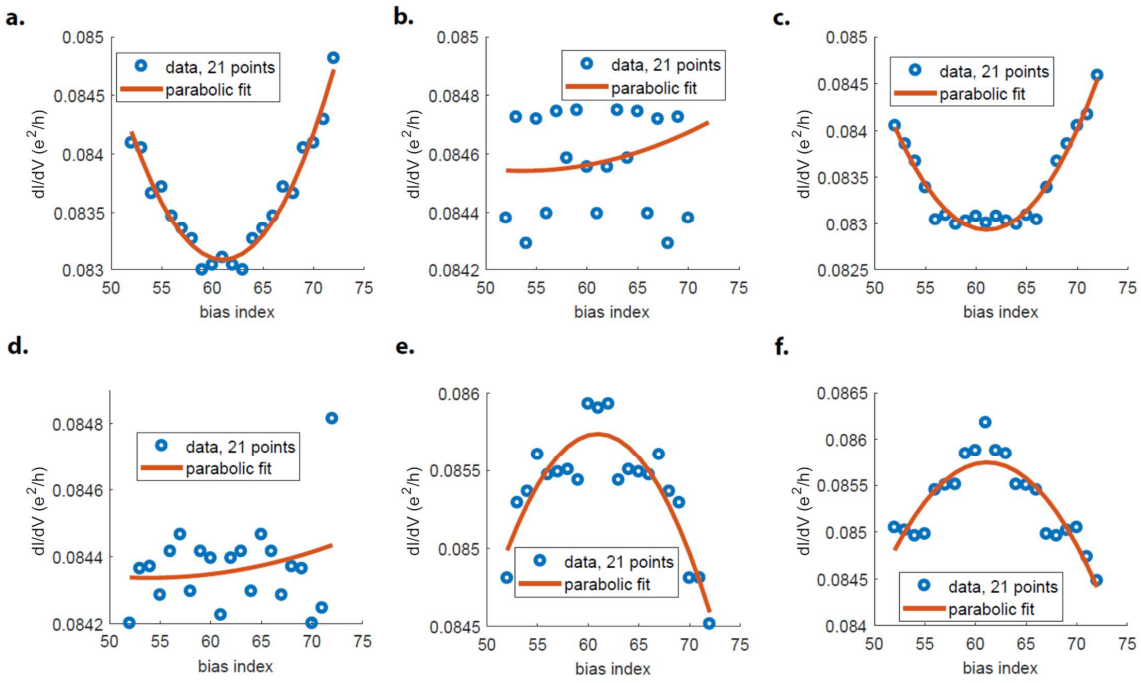

Figure S9 Extracting the curvature of zero-energy peaks using parabolic fits.

Shown above are a few examples of extracting the curvature of zero-energy peaks using parabolic fits, at B_x =0.8 T, demonstrating the fitting procedure works nicely for a well-defined peak (dip), producing a negative (positive) curvature. Yet, the parabolic fit works not so well when the curve is flat in this region, in which case it yields a small curvature, as desired.

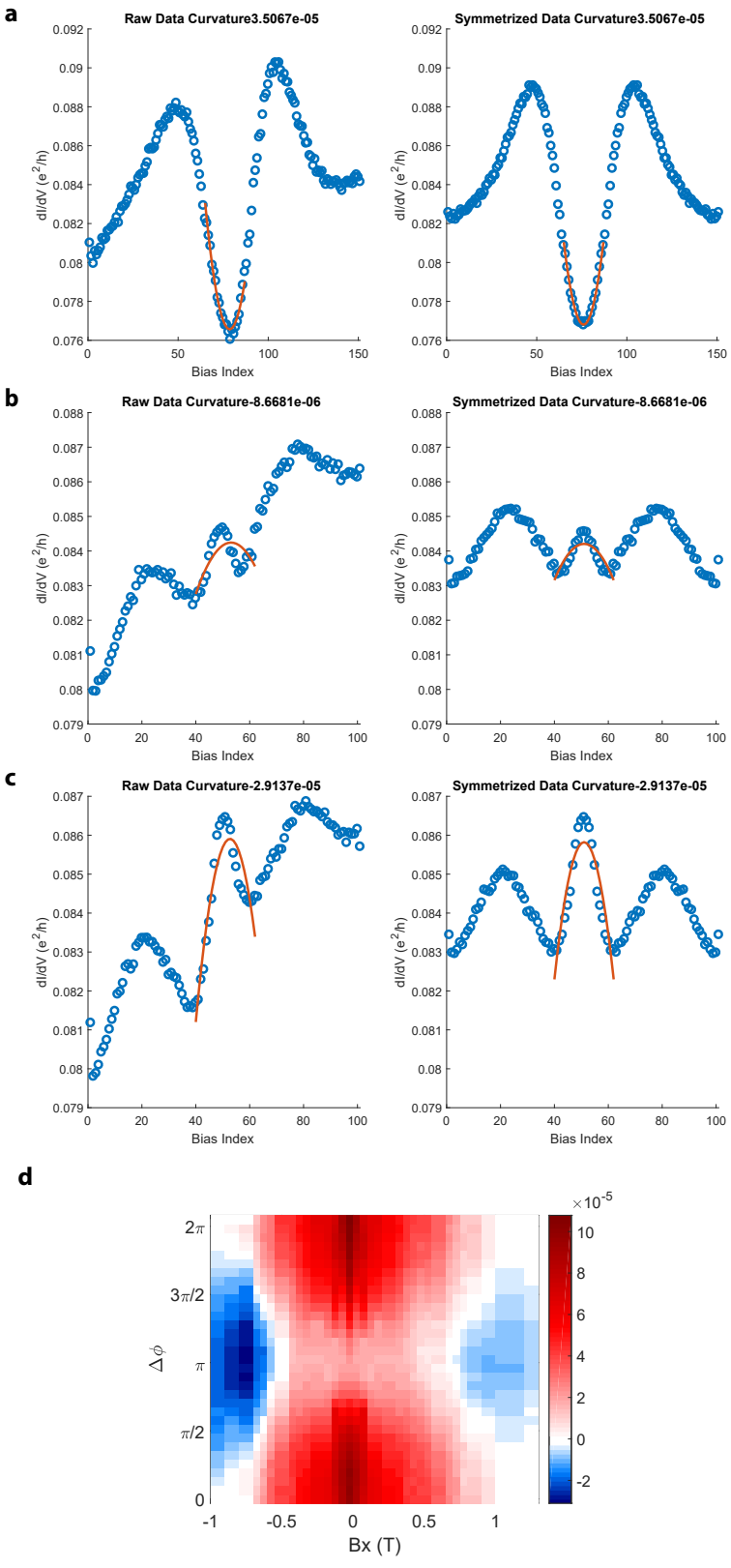
a
Raw Data Curvature3.5067e-05
Symmetrized Data Curvature3.5067e-05
b
Raw Data Curvature-8.6681e-06
Symmetrized Data Curvature-8.6681e-06
c
Raw Data Curvature-2.9137e-05
Symmetrized Data Curvature-2.9137e-05
dI/dV (e²/h)
Bias Index
d
Δ'ϕ
2π
3π/2
π
π/2
0
-1
-0.5
0
0.5
1
Bx (T)
×10⁻⁵
10
8
6
4
2
0
-2

Figure S10 Extracted zero-energy curvatures from raw data versus symmetrized data. a-c, Shown here are three examples of extracting the curvature of zero-energy peaks using parabolic fits, from the raw conductance data on the left, and from the symmetrized conductance data on the right. They show the same results becasue the curvature, which is the second order coefficient, is unchanged by the symmetrizing process. d, The zero-bias curvature extracted from the symmetrized data, as a function of both the in-plane magnetic field B_x and phase difference offset $\Delta\phi$, shown in units of $e^2/h \cdot \mu\text{eV}^{-2}$, which produces the same graph as extracted from the raw data.

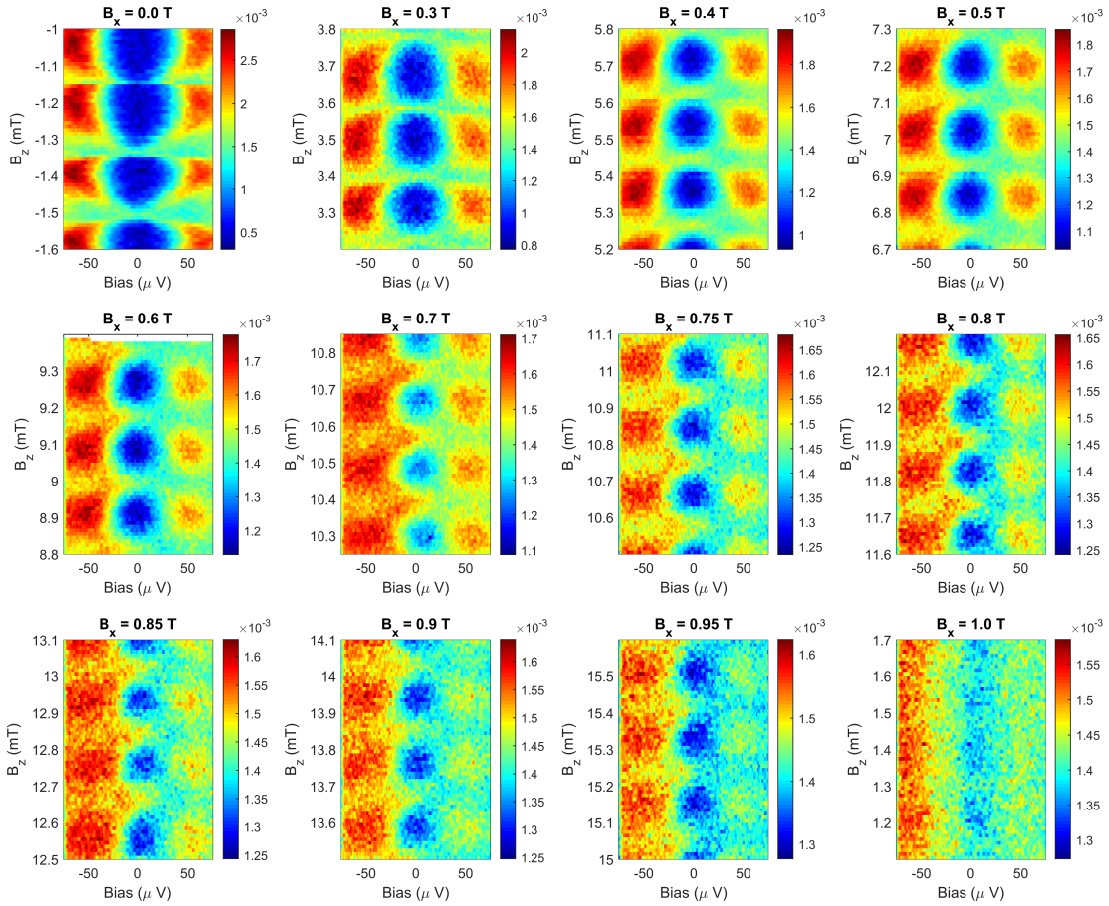

Figure S11 Differential conductance colourmaps of device Kappa at various B_x values. Shown here is the raw data for a series of two-dimensional tunneling conductance maps as a function of the bias voltage and the perpendicular field B_z, as the in-plane field B_x increases from 0 T to 1.0 T. All plots are in units of e^2/h and span over a range of 0.6 mT in B_z.

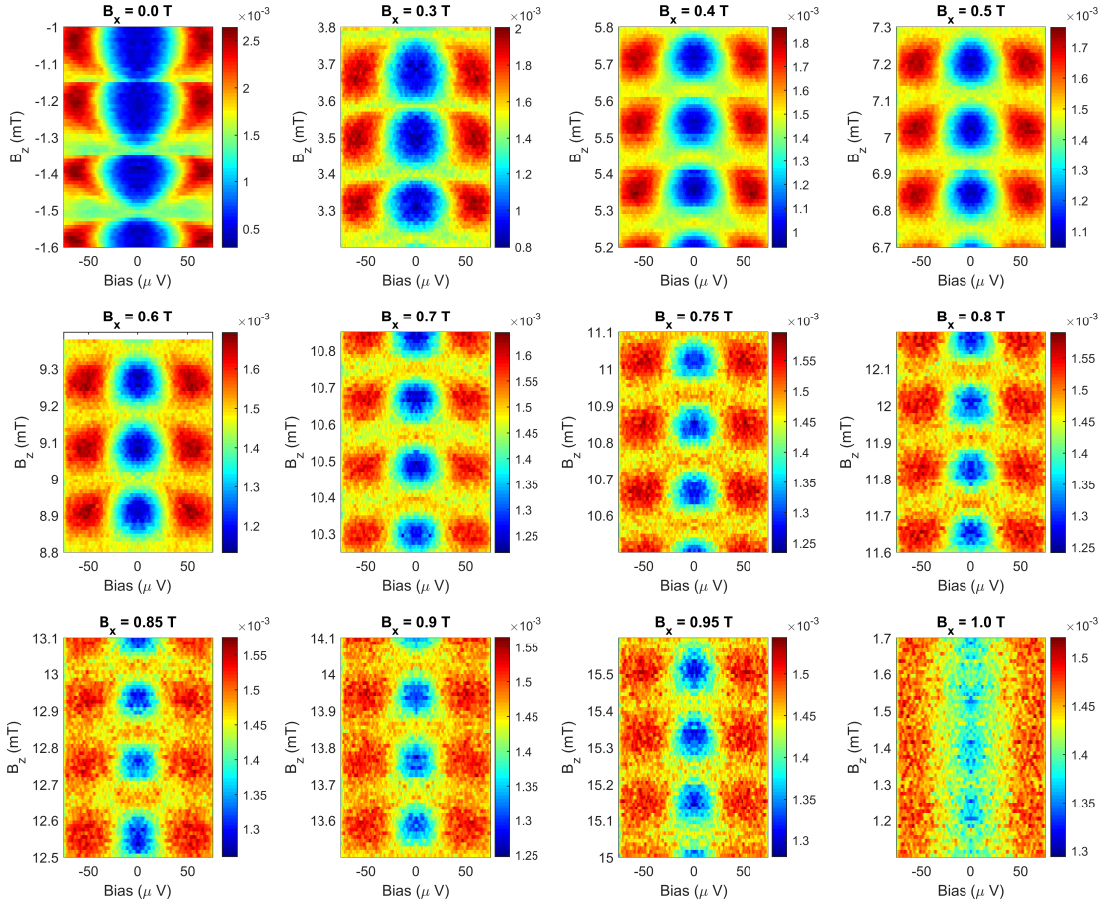

Figure S12 Symmetrized differential conductance colourmaps of device Kappa at various B_x values. Shown here is the symmetrized data for a series of two-dimensional tunneling conductance maps as a function of the bias voltage and the perpendicular field B_z, as the in-plane field B_x increases from 0 T to 1.0 T. All plots are in units of e^2/h and span over a range of 0.6 mT in B_z.

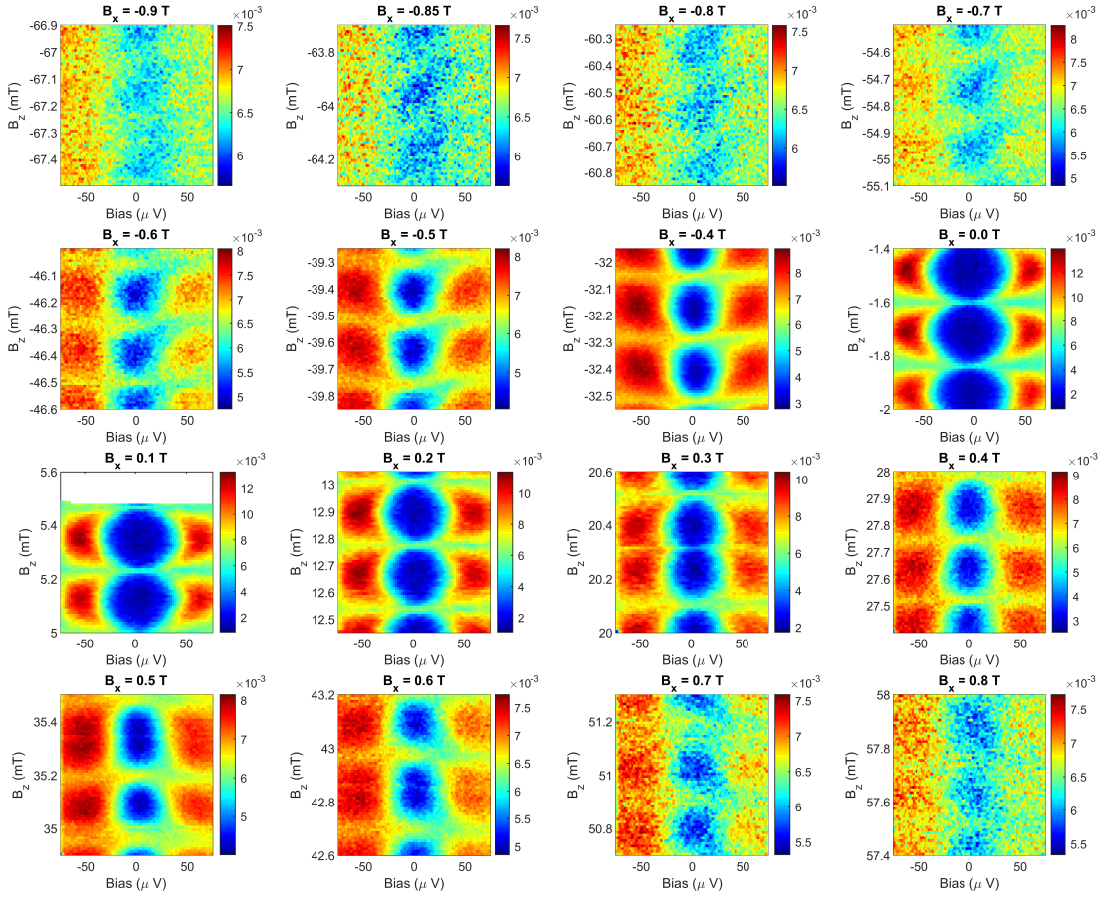

Figure S13 Differential conductance colourmaps of device Zeta at various B_x values. Shown here is the raw data for a series of two-dimensional tunneling conductance maps, as the in-plane field B_x ranges from -0.9 T to 0.8T. All plots are in units of e^2/h and span over a range of 0.6 mT.

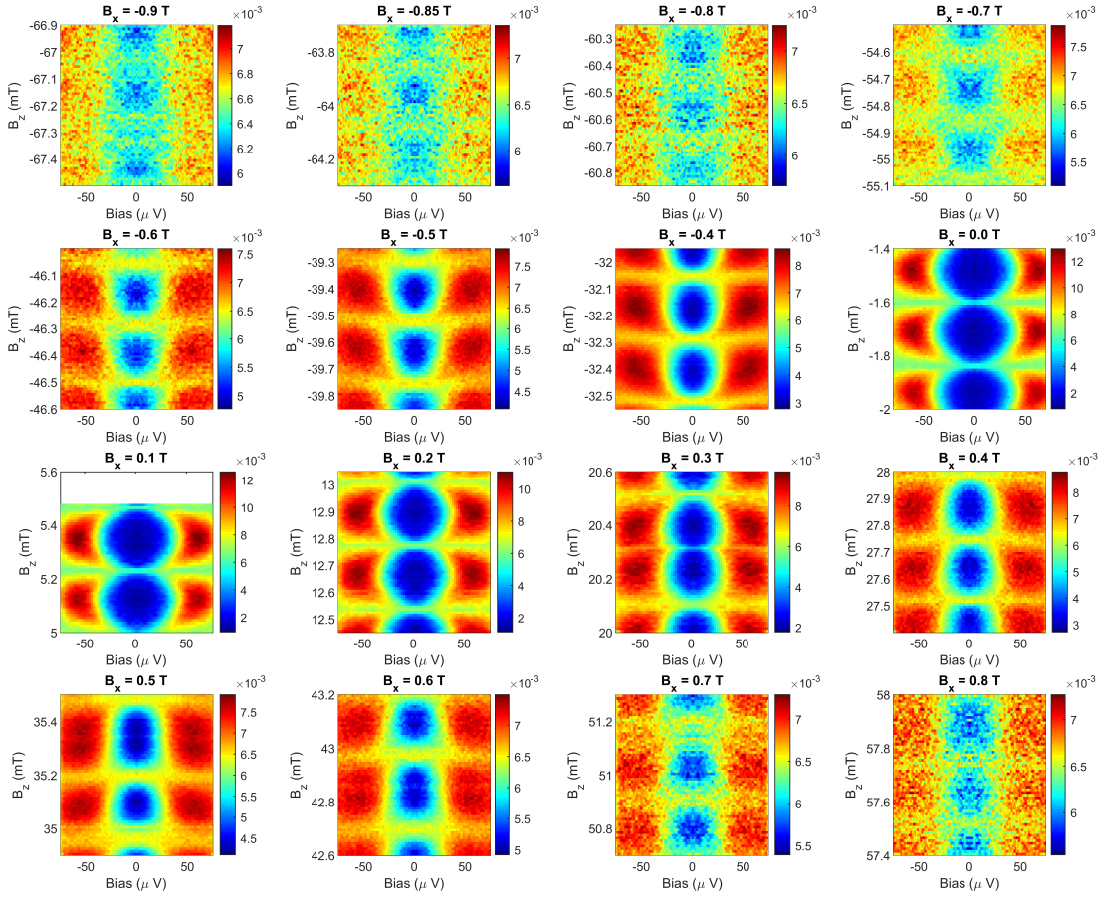

Figure S14 Symmetrized differential conductance colourmaps of device Zeta at various B_x values. Shown here is the symmetrized data for a series of two-dimensional tunneling conductance maps, as the in-plane field B_x ranges from -0.9 T to 0.8T. All plots are in units of e^2/h and span over a range of 0.6 mT in B_z.

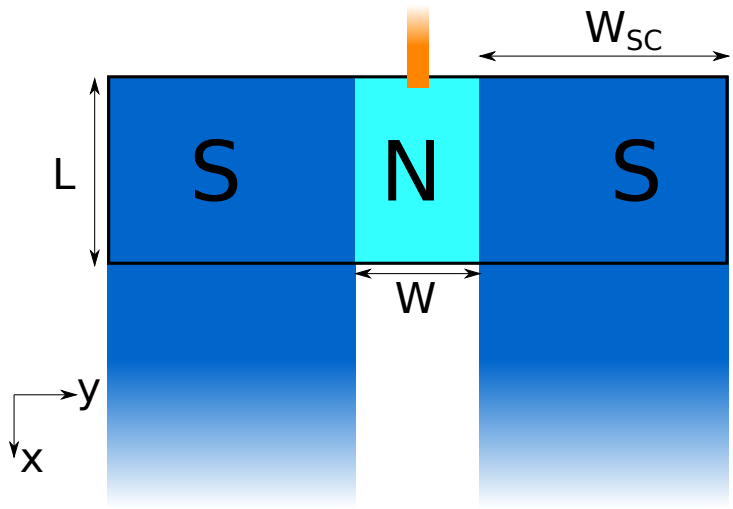

Figure S15 Setup modeled in the numerical calculations. The system comprises a rectangular region with a normal and two superconducting segments (black contour). To calculate the conductance, we add a semi-infinite normal lead in the junction center near the upper edge (orange) and two semi-infinite superconducting leads contacting the superconducting segments at the bottom edge.

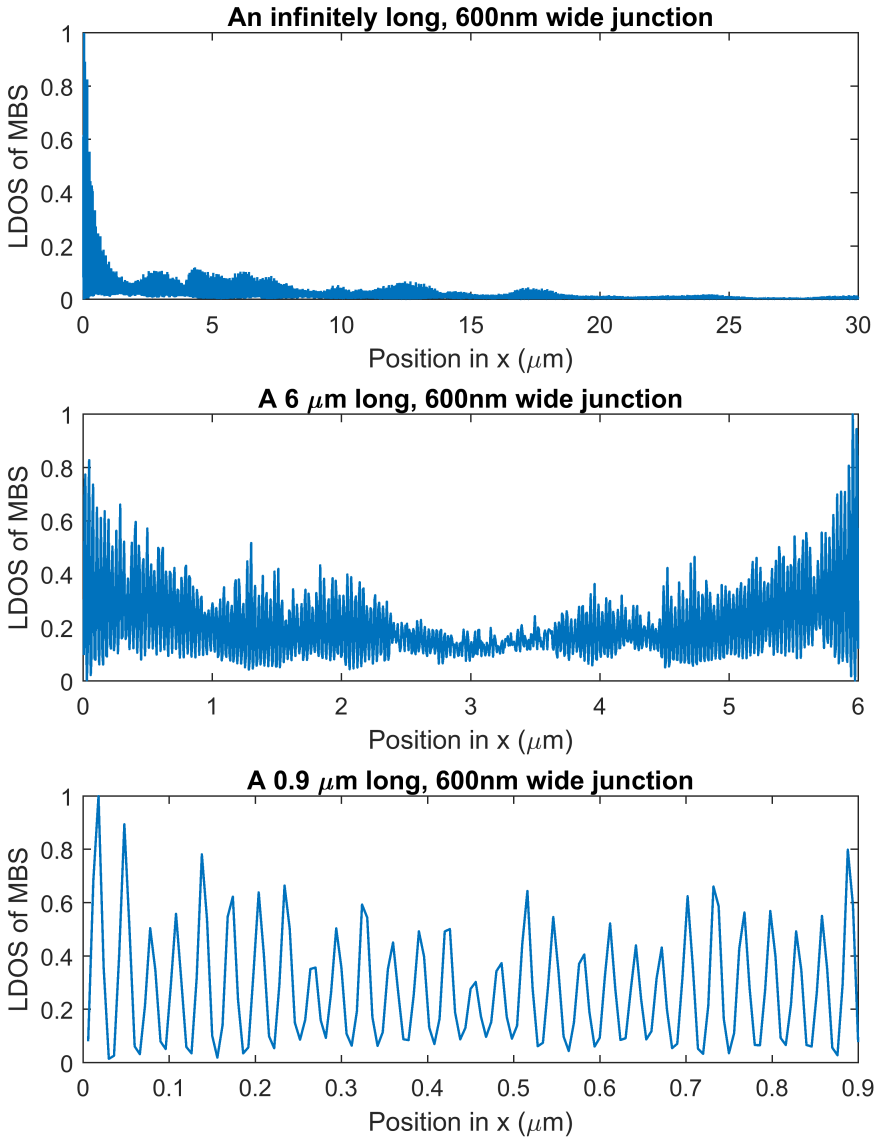

Figure S16 Delocalization of the Majorana bound state. Normalized local density of states of the lowest energy excitation, averaged over the width of the junction, as a function of distance from the edge in the setup of Figure S15 with $W = 600\,\text{nm}$ and (a) $L = \infty$, (b) $L = 6\,\mu\text{m}$, and (c) $L = 900\,\text{nm}$.

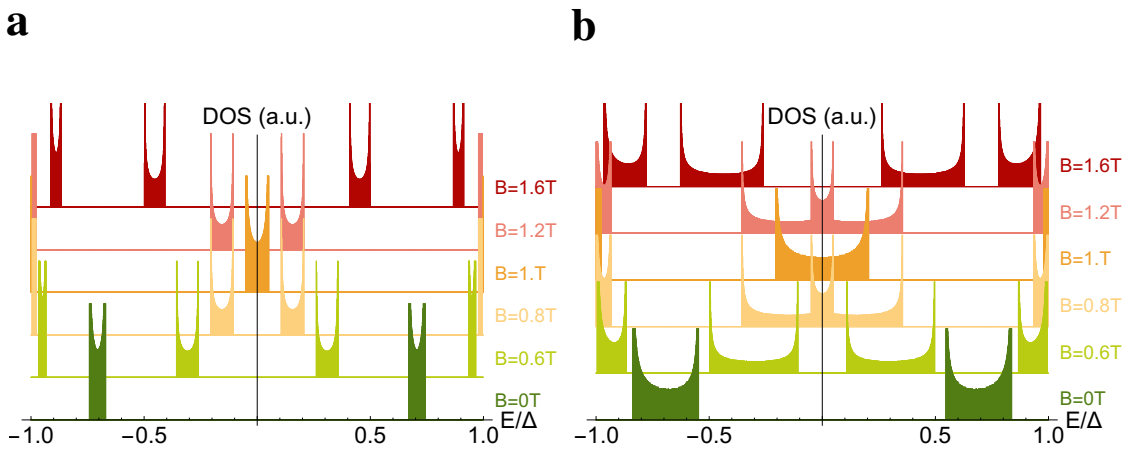

Figure S17 Calculated density of states of the Andreev band. Density of states of the Andreev band calculated from the approximate expression in Eqs. (11) and (12) for various values of the magnetic field. The superconducting phase difference is chosen as $\phi = \pi/2$ and the normal reflection probability is a) $r^2 = 0.1$ and b) $r^2 = 0.4$. We assume $k_F W \gg 1$ so that the DOS is independent of φ_N. The other parameters are chosen as above. This choice implies that the phase transition for $\phi = \pi/2$ and $r = 0$ occurs at $B = 1\,\mathrm{T}$ where $E_Z = E_T/2$.

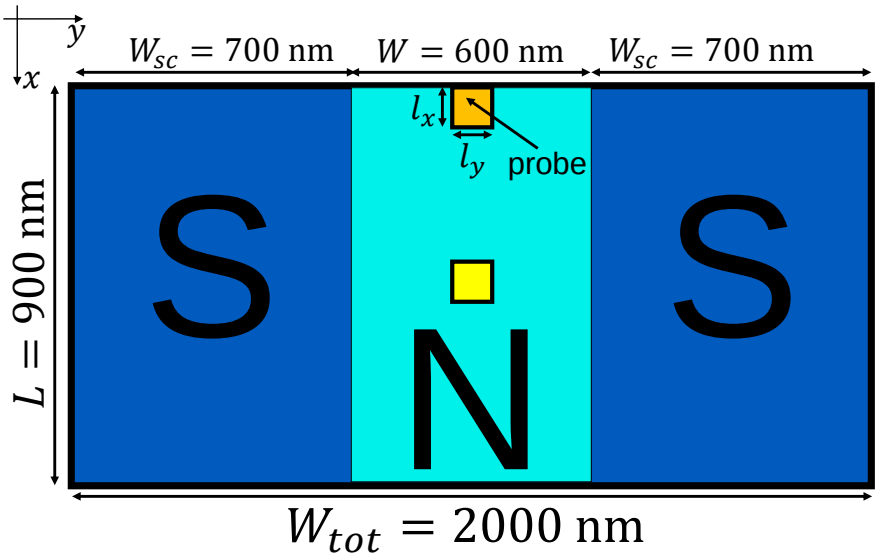

Figure S18 Setup considered for the complementary finite-difference eigenstate calculations. The system consists of a normal region of dimensions 900 nm $\times 600$ nm and two adjacent superconducting regions of dimensions 900 nm $\times 700$ nm. A phase difference of ϕ is applied between the two superconductors. The edge local density of states (LDOS) is calculated for an area of dimensions 100 nm $\times 100$ nm at the top edge of the normal region (orange area). The LDOS in the bulk is computed from a 100 nm $\times 100$ nm square in the center of the normal region (yellow area).

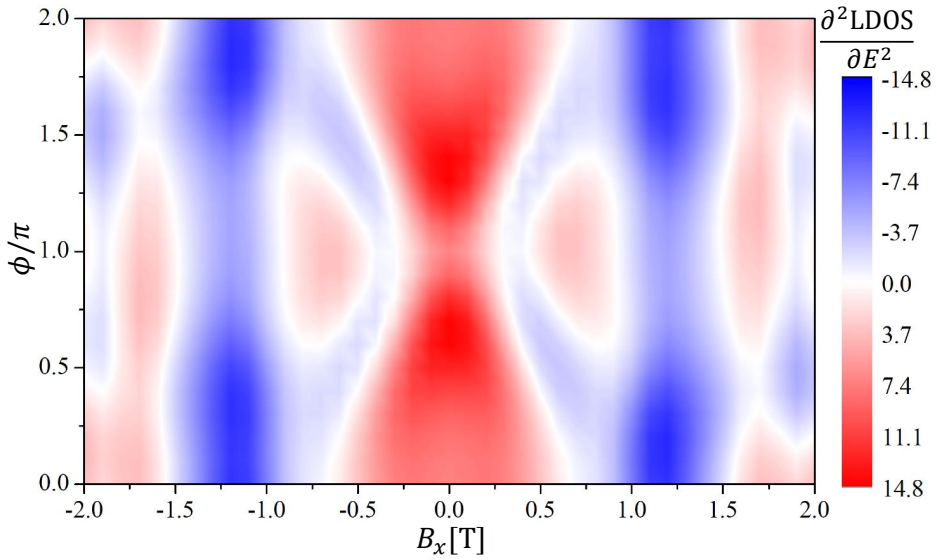

Figure S19 Predicted zero-bias curvature for a 600-nm junction. Calculated $\partial^2\mathrm{LDOS}/\partial E^2$ (in a.u.) at $E = 0$ as a function of magnetic field B_x and the phase difference ϕ between the superconducting regions for the setup illustrated in Figure S18. The area over which the LDOS is computed corresponds to a probe size of 100 nm $\times 100$ nm at the upper edge of the normal region (orange area in Figure S18).

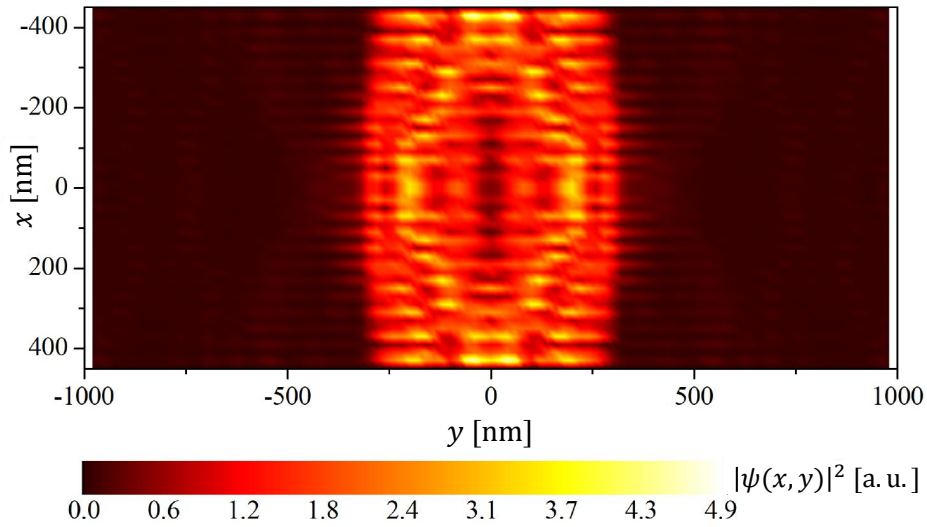

Figure S20 Wavefunction of the low-energy state for a 600-nm junction.

Probability amplitudes $|\Psi(x,y)|^2$ of the low-energy state, calculated at $B_x = 1.2$ T and $\phi = \pi$.

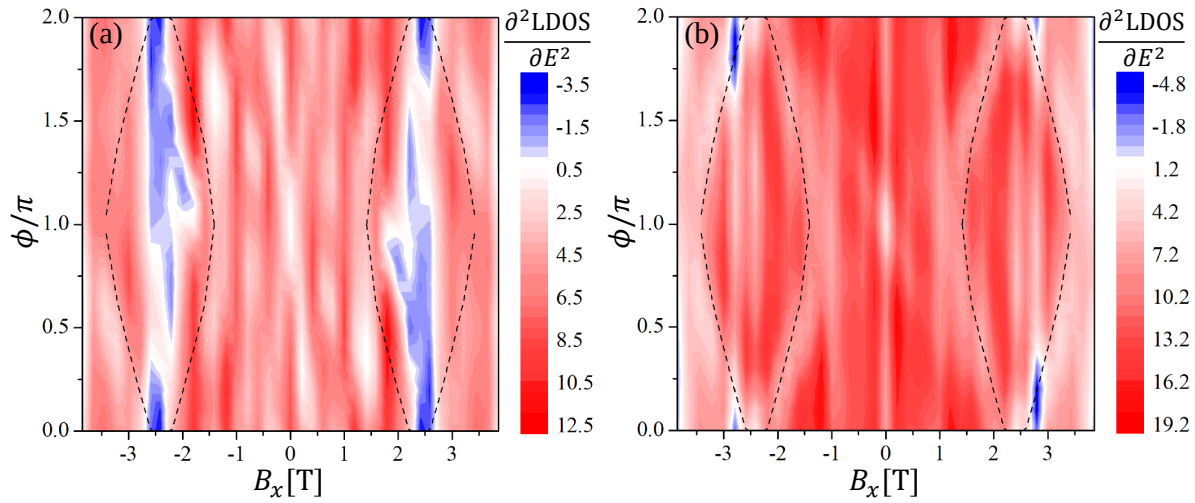

Figure S21 Predicted zero-bias curvature for a 400-nm junction. Calculated $\partial^2\mathrm{LDOS}/\partial E^2$ (in a.u.) at $E = 0$ for a Josephson junction of width $W = 400$ nm as a function of magnetic field B_x and the phase difference ϕ between the superconducting regions. Panel (a) shows the LDOS computed from a $100\mathrm{nm}\times100\mathrm{nm}$ area at the upper edge of the normal region (orange area in Figure S18). Panel (b) shows the LDOS computed from a $100\mathrm{nm}\times100\mathrm{nm}$ area in the center of the normal region (yellow area in Figure S18). The dashed lines indicate the boundaries of the topological phase obtained from an infinitely long junction $L \to \infty$.

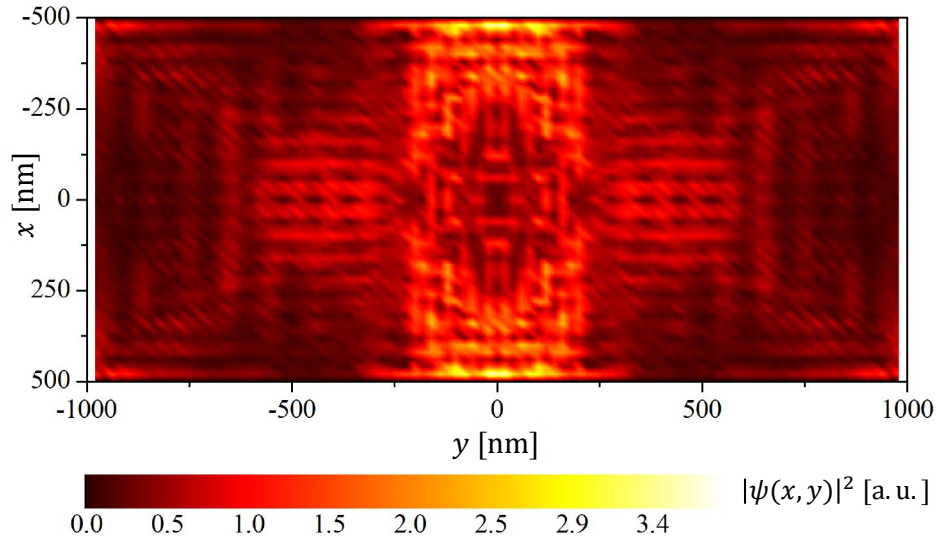

Figure S22 Wavefunction of the low-energy state for a 400-nm junction. Probability amplitudes $|\Psi(x,y)|^2$ of the low-energy state at $B_x = 2.4$ T and $\phi = 1.8\pi$.